

Self-assembled nanostructures in ionic liquids facilitate charge storage at electrified interfaces

Xianwen Mao^{1,10*}, Paul Brown¹, Ctirad Červinka^{2,3}, Gavin Hazell⁴, Hua Li^{5,6}, Yinying Ren¹, Di Chen⁷, Rob Atkin⁶, Julian Eastoe⁸, Isabelle Grillo⁹, Agilio. A. H. Padua^{1,2}, Margarida. F. Costa Gomes^{1,2*} and T. Alan Hatton^{1*}

Driven by the potential applications of ionic liquids (ILs) in many emerging electrochemical technologies, recent research efforts have been directed at understanding the complex ion ordering in these systems, to uncover novel energy storage mechanisms at IL-electrode interfaces. Here, we discover that surface-active ILs (SAILs), which contain amphiphilic structures inducing self-assembly, exhibit enhanced charge storage performance at electrified surfaces. Unlike conventional non-amphiphilic ILs, for which ion distribution is dominated by Coulombic interactions, SAILs exhibit significant and competing van der Waals interactions owing to the non-polar surfactant tails, leading to unusual interfacial ion distributions. We reveal that, at an intermediate degree of electrode polarization, SAILs display optimum performance, because the low-charge-density alkyl tails are effectively excluded from the electrode surfaces, whereas the formation of non-polar domains along the surface suppresses undesired overscreening effects. This work represents a crucial step towards understanding the unique interfacial behaviour and electrochemical properties of amphiphilic liquid systems showing long-range ordering, and offers insights into the design principles for high-energy-density electrolytes based on spontaneous self-assembly behaviour.

Research interest in ionic liquids (ILs) as electrolytes for energy devices stems from several unique properties, such as low volatility and flammability, as well as high electrochemical stability^{1–5}. An understanding of the molecular-level interactions between ILs and electrified interfaces is crucial for optimization of device performance⁶. For instance, interfacial IL layers at charged surfaces govern the electric double-layer (EDL) structure—a key factor determining the device energy density^{2,4,6,7}. The EDL structure with ILs is drastically different from that in aqueous and organic electrolytes^{8–10}; the complex ion ordering in ILs exhibits many subtleties, and remains an active area of debate^{11–14}. Here, we present the first detailed investigation into electrocapacitive characteristics and fundamental EDL structures of an emerging IL class based on surface-active agents, or surface-active ILs (SAILs)^{13,15–19}. Our study reveals a novel material design principle for enhancing charge storage owing to the self-assembled nanostructures in amphiphilic liquids, and introduces a class of liquids with long-range ordering, having broad implications for diverse fields, ranging from interfacial science^{20,21} to energy technologies^{22,23}.

SAILs are inherently amphiphilic, and can self-assemble into nanostructures composed of distinct polar and non-polar domains^{13,15–19}. Most previous studies on the IL EDL structure and IL-based energy devices focus on non-amphiphilic ILs (NAILs), where neither ion is based on a classical surfactant structure^{6,24}. Whereas nanostructuring was observed under confinement for some NAILs where one of the ions (usually the cation) bears moderate to long chains²⁵, these nanostructures are weaker (less well defined) than those for SAILs.

The bulk-phase self-assembled nanostructures of SAILs have been studied previously¹⁷, but how these nanostructures behave at electrified interfaces and are related to EDL structures critical for energy storage applications remains unexplored. Compared with NAILs, SAILs have different properties that challenge the traditional understanding of IL electrochemistry, as speculated previously²⁶. Here, we show that at elevated temperatures SAILs impart much higher capacitances than NAILs. Molecular dynamics simulations reveal that the ion distribution, cation–anion correlations and decay lengths of molecular layering of SAILs are fundamentally different from those of NAILs. The unusual EDL structure of SAILs stems from their unique ability to self-assemble into highly ordered interfacial nanostructures, which is key for producing high capacitances at intermediate electrode polarizations. The energy densities achievable with neat SAILs at elevated temperatures, or of SAIL–NAIL mixtures at room temperature, exceed those of many known electrolytes (Supplementary Note 6), showing the adaptability of SAILs for high-energy-density devices. This proof-of-concept work represents an approach for electrochemical energy storage, through the exploitation of the unfavourable interactions between hydrocarbon groups and ionic moieties in amphiphilic electrolytes, to drive the partitioning of counterions near the interface, and hence reduce the EDL thicknesses.

Bulk-phase structural and electrochemical characterization

The SAIL examined here is 1-butyl-3-methylimidazolium 1,4-bis(2-ethylhexoxy)-1,4-dioxobutane-2-sulfonate ([C₄C₁Im][AOT]) (Fig. 1a). [AOT][–] is distinctly amphiphilic, with a negative charge located

¹Department of Chemical Engineering, Massachusetts Institute of Technology, Cambridge, MA, USA. ²Laboratoire de Chimie, Ecole Normale Supérieure de Lyon and CNRS, Lyon, France. ³Department of Physical Chemistry, University of Chemistry and Technology, Prague, Czech Republic. ⁴Department of Natural Sciences, University of Chester, Chester, UK. ⁵Centre for Microscopy, Characterisation and Analysis, The University of Western Australia, Perth, Western Australia, Australia. ⁶School of Molecular Sciences, The University of Western Australia, Perth, Western Australia, Australia. ⁷Department of Materials Science and Engineering, Stanford University, Stanford, CA, USA. ⁸School of Chemistry, University of Bristol, Bristol, UK. ⁹Institut Laue-Langevin, Grenoble, France. ¹⁰Present address: Department of Chemistry and Chemical Biology, Cornell University, Ithaca, NY, USA. *e-mail: xmao@mit.edu; margarida.costa-gomes@ens-lyon.fr; tahatton@mit.edu

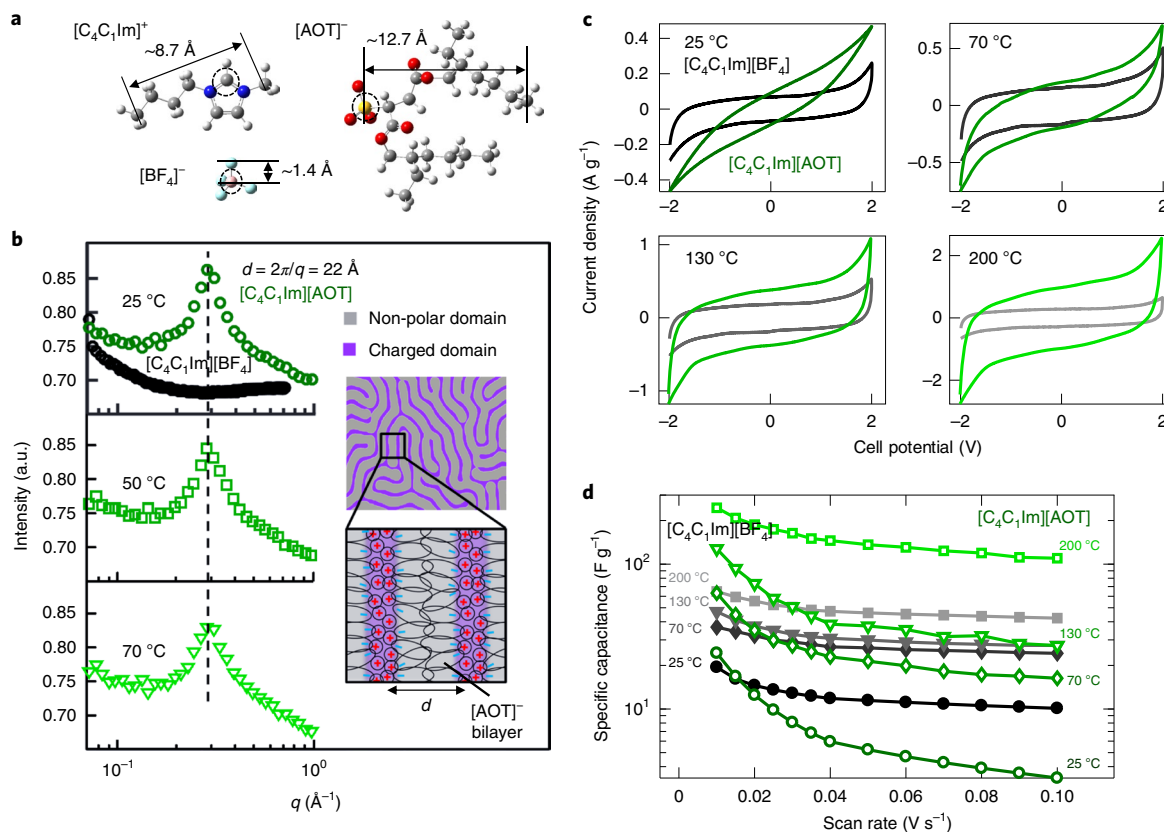


Fig. 1 | Bulk-phase structural and electrochemical characterization of $[C_4C_1Im][AOT]$. **a**, Molecular structures of $[C_4C_1Im]^+$, $[BF_4]^-$ and $[AOT]^-$ (H, white; C, grey; N, blue; S, yellow; O, red; B, pink; F, cyan). Typical distances within the molecular ions are indicated. **b**, SANS profiles of $[C_4C_1Im][BF_4]$ (25 °C) and $[C_4C_1Im][AOT]$ (25, 50 and 70 °C). Inset: illustration of self-assembly of $[C_4C_1Im][AOT]$ leading to a repeating nanostructure comprising $[AOT]^-$ bilayers (red, cation; blue, anion). Simulated SANS profiles (Supplementary Fig. 11) are consistent with the experimental data. **c, d**, Cyclic voltammogram profiles (scan rate = 20 $mV s^{-1}$) (**c**) and the specific capacitance versus the scan rate (**d**) for $[C_4C_1Im][BF_4]$ and $[C_4C_1Im][AOT]$ at 25, 70, 130 and 200 °C.

at one end of the ion (polar head) and a bulky branched di-chain hydrocarbon group at the other end (non-polar tail). The control IL is a common NAIL, $[C_4C_1Im][BF_4]$, that contains an identical cation to $[C_4C_1Im][AOT]$ but a smaller, inorganic anion. Temperature-controlled small-angle neutron scattering (SANS) measurements (Fig. 1b) show clearly that $[C_4C_1Im][AOT]$ displays a Bragg peak at $q = 0.28 \text{ \AA}^{-1}$ (q is the modulus of the scattering vector), indicating ordered nanostructures with a repeating unit length scale (d) of $\sim 22 \text{ \AA}$, consistent with the expected repeat structure for $[C_4C_1Im][AOT]$ (Fig. 1b, inset). The SANS is consistent with $[AOT]^-$ bilayers formed via aggregation of the non-polar tails, with charge-neutralizing layers of $[C_4C_1Im]^+$ adjacent to the anionic polar heads. The self-assembly of the $[AOT]^-$ non-polar tails results in the formation of nanoscale non-polar domains, whereas $[C_4C_1Im]^+$ and the $[AOT]^-$ polar heads form polar domains. In contrast, SANS from $[C_4C_1Im][BF_4]$ does not exhibit a Bragg peak, indicating the absence of any significant long-range ordered nanostructures. Figure 1c compares the cyclic voltammograms of $[C_4C_1Im][BF_4]$ and $[C_4C_1Im][AOT]$, which were obtained using supercapacitors composed of carbon nanotubes (CNTs) with a Brunauer–Emmett–Teller surface area of $198 \text{ m}^2 \text{ g}^{-1}$ (Supplementary Fig. 4a–c). At 25 °C, the cyclic voltammogram for $[C_4C_1Im][AOT]$ shows a more tilted shape and a smaller integral area than that for $[C_4C_1Im][BF_4]$. The cyclic voltammogram results suggest a higher ionic resistance and a smaller double-layer capacitance for $[C_4C_1Im][AOT]$, which may be due to its higher viscosity at this temperature (Supplementary Fig. 3c). On increasing temperature, the cyclic voltammogram integral areas for both ILs increase, consistent with reduced viscosity. However, unexpectedly,

at 130 and 200 °C, although $[C_4C_1Im][AOT]$ is still more viscous than $[C_4C_1Im][BF_4]$, the cyclic voltammograms for $[C_4C_1Im][AOT]$ now exhibit significantly larger integral areas than those for $[C_4C_1Im][BF_4]$. The cyclic voltammogram-derived specific capacitances (Fig. 1d) clearly show that at 130 and 200 °C, $[C_4C_1Im][AOT]$ possesses a remarkably better capacitive energy storage capability than does $[C_4C_1Im][BF_4]$. Control experiments show that the unusually large capacitances observed for $[C_4C_1Im][AOT]$ do not result from peculiar electrode properties or high-temperature operation-induced degradation (Supplementary Note 7).

Anomalous EDL structures in SAILS

The observed differences in electrocapacitive performance between $[C_4C_1Im][AOT]$ and $[C_4C_1Im][BF_4]$ may stem from their distinct molecular architectures, leading to different EDL structures. To understand why $[C_4C_1Im][AOT]$ outperforms $[C_4C_1Im][BF_4]$ at higher temperatures, we interrogated the detailed EDL structures of the two ILs, confined by electrified graphite surfaces at elevated temperature, via atomistic molecular dynamics simulations (details in Methods and Supplementary Note 4.1). Figure 2a,c shows the ion number density (ρ_N , normalized to the bulk value) profiles of $[C_4C_1Im][BF_4]$ and $[C_4C_1Im][AOT]$, respectively, at electrified interfaces with applied potentials (U) of $\pm 2 \text{ V}$. The NAIL $[C_4C_1Im][BF_4]$ exhibits a lamellar structure of alternating charges, which persists for around eight ion layers (four distinguishable maxima for cation and anion ρ_N profiles), consistent with previous experimental¹¹ and theoretical²⁷ observations of charged-surface-induced long-range molecular layering in common NAILS. Interestingly, $[C_4C_1Im]$

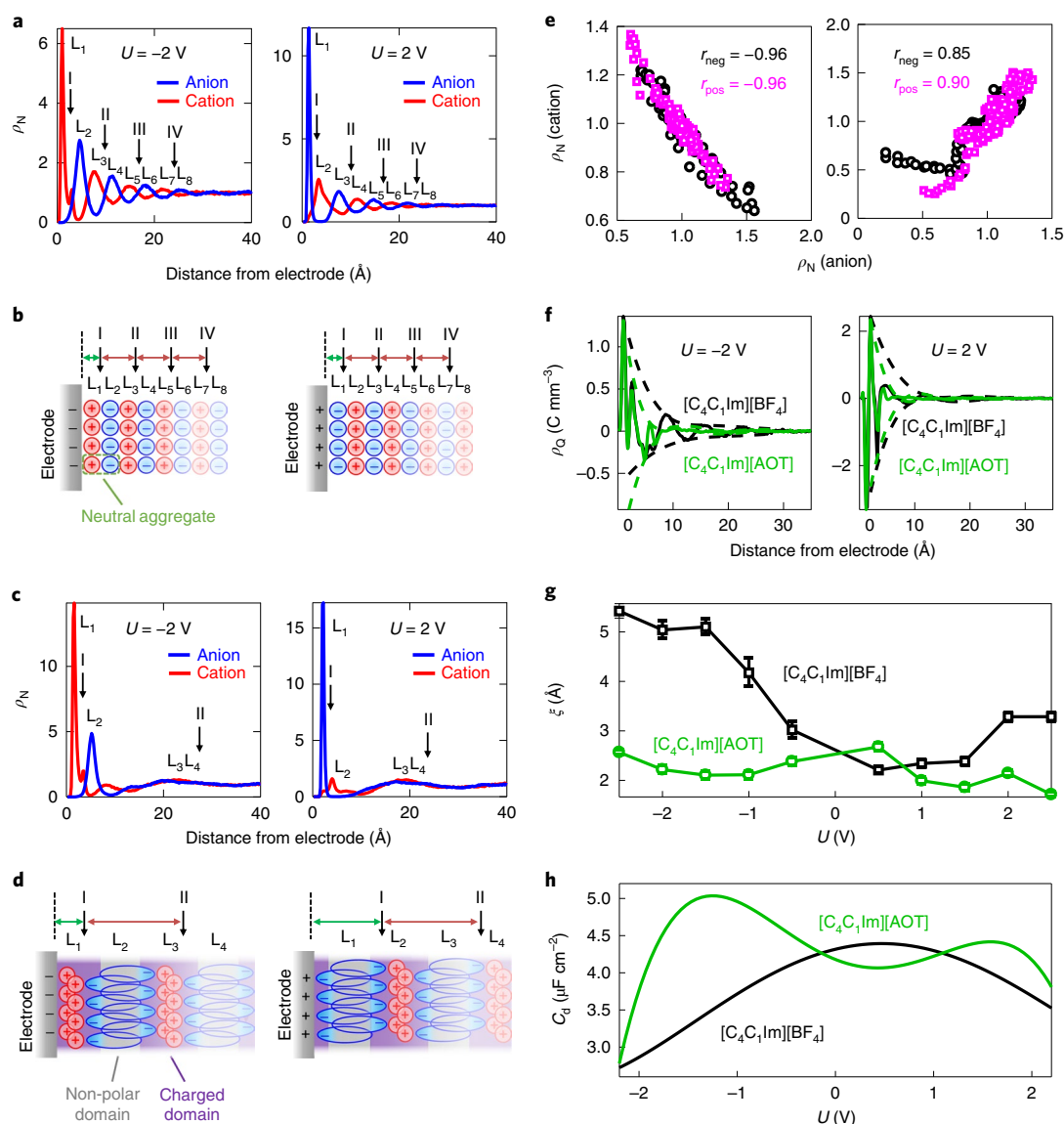


Fig. 2 | Molecular dynamics simulations reveal unusual EDL structures of [C₄C₁Im][AOT]. **a–d**, ρ_N profiles obtained from molecular dynamics simulations (**a** and **c**) and schematics (**b** and **d**) of hypothesized ion arrangements for [C₄C₁Im][BF₄] (**a** and **b**) and [C₄C₁Im][AOT] (**c** and **d**) at negatively (left panels) and positively charged interfaces (right panels) with $U = \pm 2$ V. Black arrows with I, II, III and IV indicate the possible positions corresponding to the AFM push-through locations (Fig. 3). **e**, Correlations between the cationic and anionic ρ_N values obtained at positively (magenta, $U = 2$ V) and negatively charged interfaces (black, $U = -2$ V) for [C₄C₁Im][BF₄] (left panel) and [C₄C₁Im][AOT] (right panel) for the distance range of 10–40 Å away from the interface. r_{neg} and r_{pos} are the Pearson correlation coefficients for negatively and positively charged interfaces, respectively. **f**, ρ_O profiles (solid lines) and corresponding envelope functions (dashed lines) of [C₄C₁Im][BF₄] and [C₄C₁Im][AOT] at negatively (left panel, $U = -2$ V) and positively charged interfaces (right panel, $U = 2$ V). **g, h**, Decay length (ξ) of the surface-induced ion layering (**g**) and differential capacitance (C_d ; **h**) as a function of U for [C₄C₁Im][BF₄] and [C₄C₁Im][AOT].

[AOT] displays a different molecular layering behaviour: the surface-induced charge-alternating structure for [C₄C₁Im][AOT] only persists for around two ion layers, with the first peak showing a much larger ρ_N relative to that of [C₄C₁Im][BF₄]. Notably, the simulated static neutron scattering structure factors for [C₄C₁Im][AOT] and [C₄C₁Im][BF₄] (Supplementary Fig. 11 and Supplementary Note 4.1) match their respective SANS profiles (Fig. 1b).

The nanoscale self-assembly of the non-polar groups in [C₄C₁Im][AOT] may account for the atypical ion packing behaviour at electrified interfaces (Fig. 2c,d), being in stark contrast with the conventional behaviour of NAILs (Fig. 2a,b). At neutral interfaces, the bulk microscopic structure of [C₄C₁Im][AOT] is characterized

by the formation of charged polar domains and non-polar domains (Fig. 1b, inset). The introduction of surface charges then induces alignment of the charged domains along the interface. Near a positively charged surface, the polar heads of [AOT]⁻ are electrostatically attracted to the interface, whereas the non-polar tails orientate outward, in close proximity to the next [AOT]⁻ layer, thus forming a bilayer parallel to the positively charged surface, with a neutralizing [C₄C₁Im]⁺ layer adjacent to the anionic polar heads of [AOT]⁻. At a negatively charged surface, the innermost ion layer is enriched in [C₄C₁Im]⁺ cations, which fully neutralize the adjacent anionic [AOT]⁻ bilayer (that is, the presence of an [AOT]⁻ bilayer squeezes excess cations into the first ion layer

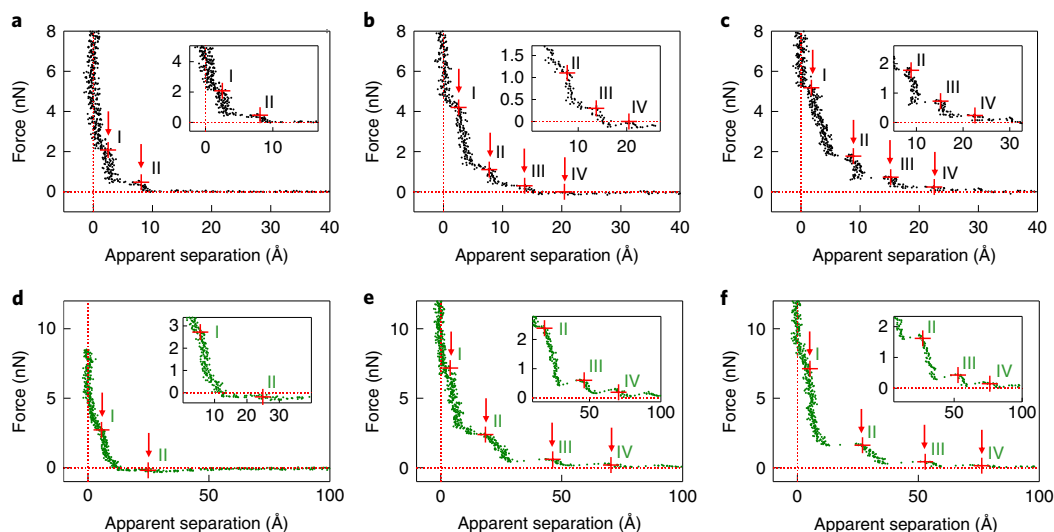


Fig. 3 | Elucidation of interfacial molecular layering through AFM force measurements. **a–f**, Force versus apparent separation profiles obtained with a silica colloid probe approaching a graphite electrode surface immersed in [C₄C₁Im][BF₄] (**a–c**) or [C₄C₁Im][AOT] (**d–f**) at OCP (**a** and **d**), OCP-1V (**b** and **e**) and OCP+1V (**c** and **f**). Insets: magnified views of the lower force regimes. Red crosses marked I, II, III or IV indicate the locations of each discrete step and the ‘rupture force’ magnitudes.

near the interface). The ability to pack excess ions at charged interfaces is an advantageous feature of SAILs compared with NAILs, and is driven by the unfavourable interaction between the hydrocarbon and ionic groups compared with cation–anion interactions. Another unexpected finding for [C₄C₁Im][AOT] is that the cation and anion ρ_N profiles beyond the first two ion layers are positively correlated (Fig. 2e, right panel), possibly due to the co-movement of [C₄C₁Im]⁺ cations and [AOT]⁻ polar heads. The non-polar tail–tail interaction could lead to the confinement of small [C₄C₁Im]⁺ cations and [AOT]⁻ polar heads within the polar domains. With short-alkyl-chain NAILs, which cannot self-assemble, the ion–ion electrostatic interactions alone dictate that the anionic density reaches a maximum where the cationic density reaches a minimum, which should result in negatively correlated anion–cation spatial distributions (Fig. 2e, left panel).

The ability of [C₄C₁Im][AOT] to pack excess ions at the interface, and the positive correlation between the cation and anion spatial distributions, suggest that [C₄C₁Im][AOT] should reach bulk electroneutrality over shorter distances than [C₄C₁Im][BF₄], which can be validated by calculating the net charge density (ρ_Q) distributions (Fig. 2f). The NAIL [C₄C₁Im][BF₄] shows a pronounced ρ_Q oscillatory pattern before reaching electroneutrality at around 30 Å from the surface. In contrast, the amplitude of ρ_Q oscillation for [C₄C₁Im][AOT] diminishes more quickly, and decays to its bulk value around 10 Å from the surface. The decay length (ξ) of the charge oscillation, quantified using an envelope function that confines the ρ_Q profile (Supplementary Note 4.2), is shown in Fig. 2g as a function of U . Compared with [C₄C₁Im][BF₄], [C₄C₁Im][AOT] generally exhibits smaller ξ values, indicating thinner EDLs and thus larger capacitances. The calculated differential capacitances (C_d) (Fig. 2h and Supplementary Note 4.2) show that, with intermediate electrode polarization (that is, $1\text{ V} < |U| < 2\text{ V}$), [C₄C₁Im][AOT] generally exhibits higher differential capacitances than does [C₄C₁Im][BF₄]. However, at low electrode polarization (that is, U is near 0 V), [C₄C₁Im][AOT] shows lower capacitances than [C₄C₁Im][BF₄], probably because near the electrode surface the former has a larger density of [AOT]⁻ non-polar tails (that is, latent voids), reducing the near-surface charge density (Supplementary Fig. 12). In contrast, at intermediate polarization (that is, $|U|$ is about 1–2 V), those non-polar tails do not partition to the electrode surface (Supplementary

Fig. 12), resulting in ~22-Å-wide non-polar domains parallel to the electrode surface. This prevents the development of a strongly oscillating, cation–anion alternating structure, commonly observed in NAILs, that would lead to overscreening and EDL thickening. The role of such non-polar domains in preventing overscreening effects may be analogous to that played by a second electrode wall inside a nanopore²⁸. The potential-dependent rearrangement of the [AOT]⁻ non-polar tails, revealed by these atomistic molecular dynamics simulations, agrees with earlier studies based on Monte Carlo simulations of liquids with elongated ions containing charged ‘heads’ and neutral ‘tails’^{29,30}. At high electrode polarization (that is, $|U| > 2\text{ V}$), lattice saturation effects due to the steric constraints of finite ion sizes^{6,7} occur, and the capacitances of both [C₄C₁Im][AOT] and [C₄C₁Im][BF₄] decrease. Additionally, the thinner EDL (and thus shorter Debye length) for [C₄C₁Im][AOT] relative to that of [C₄C₁Im][BF₄] at intermediate electrode polarization implies a higher free ion concentration in [C₄C₁Im][AOT]. In the EDL of [C₄C₁Im][BF₄], as in other NAILs^{8,10}, most cations and anions are strongly associated to form ‘neutral aggregates’ (Fig. 2b), which contribute weakly to the free ion concentration. In contrast, in the EDL of [C₄C₁Im][AOT], due to its amphiphilic nature, only half of the population of the first counterion layer could form neutral aggregates with the neighbouring co-ion layer, resulting in abundant free counterions at the interface (Fig. 2d). Additional constant surface charge simulations (Supplementary Fig. 7) yielded consistent results with those shown here by the constant surface potential method (Fig. 2).

Elucidation of interfacial nanostructures

Atomic force microscopy (AFM) measurements were performed to examine the nanoscale molecular layering of these ILs at a graphite electrode (for experimental details, see Methods and Supplementary Note 5). It is recognized that ILs form layered structures near solid surfaces, which are referred to as interfacial nanostructures^{31–35}. The AFM force–distance profiles for [C₄C₁Im][BF₄] and [C₄C₁Im][AOT] (Fig. 3) consist of a series of pronounced, discrete steps, produced by the AFM tip pushing up against, and then rupturing, interfacial layers. The ‘rupture force’ for an IL layer is reflected by the maximum of each step; a larger rupture force indicates a higher degree of ordering (that is, stronger cohesive interactions) in the

ion layer. For both ILs, at the open circuit potential (OCP), the data reveal only two steps with small rupture forces, indicating weak interfacial structures, whereas with applied biases (OCP ± 1 V) at least four steps are seen, with much higher rupture forces, indicating stronger ordering of interfacial nanostructures. Additionally, for all three cases (at OCP, OCP -1 V and OCP $+1$ V), the rupture force decreases more rapidly with layer number for $[\text{C}_4\text{C}_1\text{Im}][\text{AOT}]$ than $[\text{C}_4\text{C}_1\text{Im}][\text{BF}_4]$, which closely matches the simulations described above (Fig. 2a,c). Moreover, the rupture force for step I is higher for $[\text{C}_4\text{C}_1\text{Im}][\text{AOT}]$ than for $[\text{C}_4\text{C}_1\text{Im}][\text{BF}_4]$, again consistent with the simulations (Fig. 2a,c) showing that ρ_{N} of the innermost layer is much larger for $[\text{C}_4\text{C}_1\text{Im}][\text{AOT}]$ than for $[\text{C}_4\text{C}_1\text{Im}][\text{BF}_4]$.

The separation between two adjacent steps (that is, between steps I/II, II/III or III/IV, as shown in Fig. 3) for $[\text{C}_4\text{C}_1\text{Im}][\text{BF}_4]$ and $[\text{C}_4\text{C}_1\text{Im}][\text{AOT}]$ is notably different. For $[\text{C}_4\text{C}_1\text{Im}][\text{BF}_4]$, the separation is 6–7 Å (corresponding to the physical dimension of an ion pair of $[\text{C}_4\text{C}_1\text{Im}]^+$ and $[\text{BF}_4]^-$), in accordance with the molecular dynamics simulations (Fig. 2a; schematically illustrated by orange double-headed arrows in Fig. 2b). In stark contrast, the separation between steps for $[\text{C}_4\text{C}_1\text{Im}][\text{AOT}]$ is three to four times larger (22–24 Å), in good agreement with both the repeating unit length scale measured by SANS (Fig. 1b) and the simulations (Fig. 2c; schematically illustrated by orange double-headed arrows in Fig. 2d). For $[\text{C}_4\text{C}_1\text{Im}][\text{BF}_4]$, with applied biases of ± 1 V, the separation between the electrode surface and step I (corresponding to the layer nearest to the surface) is about 2–3 Å, indicating a single ion layer (either cation or anion, depending on the applied bias, as shown by the green double arrow in Fig. 2b). This agrees well with the simulated ion number density profiles, indicating that the first ion layer is about 2–3 Å thick (Fig. 2a). For $[\text{C}_4\text{C}_1\text{Im}][\text{AOT}]$, at OCP -1 V, the separation between the electrode surface and step I is about 4 Å, corresponding to a cation-rich layer, also consistent with the simulations (Fig. 2c, left; green double-headed arrow in Fig. 2d, left). For $[\text{C}_4\text{C}_1\text{Im}][\text{AOT}]$ at OCP $+1$ V, step I is about 6 Å thick, consistent with simulations (Fig. 2c, right; green double-headed arrow in Fig. 2d, right), but much smaller than the distance expected for an $[\text{AOT}]^-$ double layer. This is a consequence of the $[\text{AOT}]^-$ neutral tails tending to orientate towards the electrode surface through solvophobic interactions (Supplementary Fig. 12). These force measurements unambiguously confirm the fundamentally different interfacial nanostructures between $[\text{C}_4\text{C}_1\text{Im}][\text{AOT}]$ and $[\text{C}_4\text{C}_1\text{Im}][\text{BF}_4]$, as suggested by the molecular dynamics simulations. While high-energy X-ray reflectivity measurements may be used to elucidate interfacial nanostructures of ILs¹¹, we could not obtain good X-ray reflectivity signals for our IL systems, possibly due to the difficulty of preparing a thin, uniform IL film with high stability under X-ray exposure (Supplementary Note 5).

EDL properties probed by impedance measurements

To further examine how the EDL capacitances of $[\text{C}_4\text{C}_1\text{Im}][\text{AOT}]$ and $[\text{C}_4\text{C}_1\text{Im}][\text{BF}_4]$ vary with applied potential, impedance measurements (Methods and Supplementary Note 3) were performed to obtain the differential capacitance versus potential profiles for both ILs (Fig. 4), using a glassy carbon electrode consisting of a flat IL-graphite interface. With increasing temperature, the capacitances of both ILs become larger, consistent with decreasing viscosities, in accordance with the cyclic voltammogram measurements in a supercapacitor device (Fig. 1d). More importantly, the capacitance curve of $[\text{C}_4\text{C}_1\text{Im}][\text{AOT}]$ is characterized by a minimum at small $|U|$ and two maxima at intermediate $|U|$, whereas that for $[\text{C}_4\text{C}_1\text{Im}][\text{BF}_4]$ exhibits a bell-like shape. These capacitance profiles for $[\text{C}_4\text{C}_1\text{Im}][\text{AOT}]$ and $[\text{C}_4\text{C}_1\text{Im}][\text{BF}_4]$ agree generally with the simulations (Fig. 2h), re-emphasizing fundamental differences in the EDL structures between SAILs and NAILs. Certain fine features, such as the exact positions of minima and maxima in the capacitance curves, differ between the simulations and experimental data, possibly

due to factors such as specific adsorption or local dielectric properties that are not accurately captured by the simulations. Notably, the experimentally measured capacitances here are not dictated by the quantum capacitances of the carbon electrodes employed, and reflect faithfully the EDL capacitances of the ILs investigated (Supplementary Note 8).

Generality, applicability and limitations of SAILs

We simulated the EDL structures of two other SAILs sharing the same $[\text{C}_4\text{C}_1\text{Im}]^+$ cation as $[\text{C}_4\text{C}_1\text{Im}][\text{AOT}]$, but with different anions: dodecylsulfonate ($[\text{DDS}]^-$ single-chain surfactant anion) and 1,5-bis(hexyloxy)-3-((hexyloxy)carbonyl)-1,5-dioxopentane-2-sulfonate ($[\text{TC}]^-$ tri-chain surfactant anion) (Fig. 5a). These other SAILs show significant structural variations compared with $[\text{AOT}]^-$. The simulations indicate that, compared with $[\text{C}_4\text{C}_1\text{Im}][\text{BF}_4]$, both $[\text{C}_4\text{C}_1\text{Im}][\text{DDS}]$ and $[\text{C}_4\text{C}_1\text{Im}][\text{TC}]$ also exhibit diminished ρ_{O} oscillations (Fig. 5b) and thinner EDLs (Fig. 5c) at intermediate electrode polarizations (that is, surface charge density $\sigma = \pm 5$ and $\pm 10 \mu\text{C cm}^{-2}$), suggesting that these may be generic features of SAILs. To validate that molecular dynamics captures the self-assembly behaviour shown by SANS, additional simulations were performed using uncharged confining surfaces at a lower temperature of 100 °C. Such conditions allow for the study of SAIL structures in the absence of an electric field, and with suppressed thermal fluctuations, so that the non-polar domains align parallel to the confining surface (Fig. 5d, left) instead of assuming random orientations (Fig. 5d, right). Therefore, the repeating structures of SAILs along the z axis normal to the interface can be visualized directly. Figure 5e shows clearly that the three SAILs (that is, $[\text{C}_4\text{C}_1\text{Im}][\text{DDS}]$, $[\text{C}_4\text{C}_1\text{Im}][\text{AOT}]$ and $[\text{C}_4\text{C}_1\text{Im}][\text{TC}]$) display a periodic ρ_{N} pattern reflecting their repeating nanostructures. This pattern is lacked by the profile for $[\text{C}_4\text{C}_1\text{Im}][\text{BF}_4]$. The average peak spacing in the ρ_{N} patterns appears to decrease from $[\text{C}_4\text{C}_1\text{Im}][\text{DDS}]$ to $[\text{C}_4\text{C}_1\text{Im}][\text{AOT}]$ to $[\text{C}_4\text{C}_1\text{Im}][\text{TC}]$, consistent with the reduction in anion size/length ($[\text{DDS}]^- > [\text{AOT}]^- > [\text{TC}]^-$), as well as the decreasing characteristic length of repeating structures measured by small-angle X-ray scattering ($[\text{C}_4\text{C}_1\text{Im}][\text{DDS}] = 22.9 \text{ \AA}$; $[\text{C}_4\text{C}_1\text{Im}][\text{AOT}] = 21.5 \text{ \AA}$; and $[\text{C}_4\text{C}_1\text{Im}][\text{TC}] = 18.8 \text{ \AA}$)¹⁹.

To validate experimentally that SAILs generally outperform NAILs at elevated temperatures, we synthesized three other SAILs (that is, $[\text{C}_4\text{C}_1\text{Im}][\text{C}_8\text{SO}_4]$, $[\text{C}_4\text{C}_1\text{Im}][\text{C}_{10}\text{SO}_4]$ and $[\text{C}_4\text{C}_1\text{Im}][\text{C}_{12}\text{SO}_4]$; Supplementary Fig. 10 and Supplementary Table 6). Their SANS profiles (Fig. 6a) at 70 °C display clear Bragg peaks at $q = 0.24$, 0.22 and 0.22 \AA^{-1} , respectively, indicating repeat structures with characteristic dimensions of 26, 28 and 28 Å, respectively. The SANS profiles at 25 and 50 °C for $[\text{C}_4\text{C}_1\text{Im}][\text{C}_8\text{SO}_4]$ and $[\text{C}_4\text{C}_1\text{Im}][\text{C}_{10}\text{SO}_4]$ are similar to those at 70 °C. The long-chain analogue $[\text{C}_4\text{C}_1\text{Im}][\text{C}_{12}\text{SO}_4]$ is solid at low temperatures (25 and 50 °C), resulting a Bragg peak at $q = 0.31 \text{ \AA}^{-1}$. Figure 6b depicts the specific capacitances (left y axes) of the three SAILs (using CNT supercapacitors), together with the enhancement (right y axes) relative to those of $[\text{C}_4\text{C}_1\text{Im}][\text{BF}_4]$. Relative to $[\text{C}_4\text{C}_1\text{Im}][\text{BF}_4]$, and at high temperature (130 °C), these SAILs exhibit larger capacitances with a two- to threefold enhancement, similar to the findings with $[\text{C}_4\text{C}_1\text{Im}][\text{AOT}]$ (Supplementary Fig. 6).

The energy storage performance of SAILs depends not only on temperature but also on the operating voltage window. For example, whether $[\text{C}_4\text{C}_1\text{Im}][\text{AOT}]$ exhibits larger or smaller differential capacitances than $[\text{C}_4\text{C}_1\text{Im}][\text{BF}_4]$ depends on the degree of electrode polarization (that is, the applied potential), as shown experimentally (Fig. 4) and also via molecular dynamics simulations (Fig. 2h). Therefore, when operating over a wide voltage window, a supercapacitor with $[\text{C}_4\text{C}_1\text{Im}][\text{AOT}]$ should show larger capacitances than if $[\text{C}_4\text{C}_1\text{Im}][\text{BF}_4]$ is used, whereas when operating over a narrow voltage window, the order is reversed. However, $[\text{C}_4\text{C}_1\text{Im}][\text{AOT}]$ is preferred for energy storage applications because in practice it is

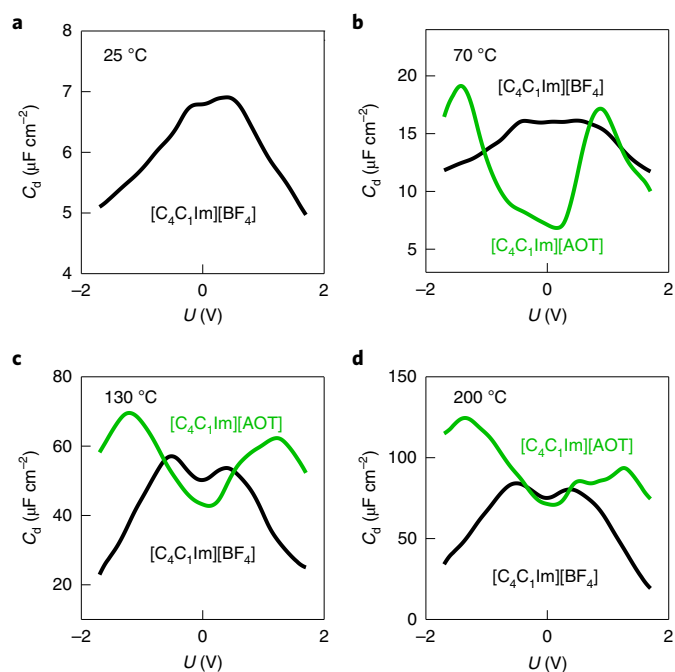


Fig. 4 | EDL properties probed by impedance measurements. a–d, Experimentally determined differential capacitances as a function of the applied potential (U , versus OCP) for $[\text{C}_4\text{C}_1\text{Im}][\text{BF}_4]$ and $[\text{C}_4\text{C}_1\text{Im}][\text{AOT}]$ at 25 °C (a), 70 °C (b), 130 °C (c) and 200 °C (d) on a glassy carbon electrode.

advantageous to have large capacitances when operating over broad voltage windows since energy density scales as $\int_0^V CU dU$ or CV^2 , where C is the capacitance, U is the applied potential and V is the operating voltage window.

The Ragone plot (Supplementary Fig. 14) shows that at low temperatures, the high viscosity of $[\text{C}_4\text{C}_1\text{Im}][\text{AOT}]$ results in energy density/power density combinations that are worse than those of $[\text{C}_4\text{C}_1\text{Im}][\text{BF}_4]$. However, at high temperatures where $[\text{C}_4\text{C}_1\text{Im}][\text{AOT}]$ is more fluid, it outperforms $[\text{C}_4\text{C}_1\text{Im}][\text{BF}_4]$ in terms of both energy and power density, making $[\text{C}_4\text{C}_1\text{Im}][\text{AOT}]$ particularly suitable for important high-temperature applications³⁶. Also, mixing $[\text{C}_4\text{C}_1\text{Im}][\text{AOT}]$ with $[\text{C}_4\text{C}_1\text{Im}][\text{BF}_4]$ led to higher capacitances than those of individual components alone at room temperature (Supplementary Fig. 9), suggesting a path to engineering SAIL-based energy devices for low-temperature uses. Due to their larger ion sizes, SAILs might not adsorb so easily into ultra-narrow pores with certain porous carbon electrodes³⁷; however, SAILs could be used in combination with other non-porous high-surface-area electrodes such as onion-like carbon³⁸, carbon nanocage³⁹ and carbon fibres^{40,41}. Moreover, the electrocapacitive performance of SAILs depends on the specific chemical structure (for example, the length of the alkyl chains), because these determine the strength of interactions between alkyl chains, as well as between the electrode surfaces and alkyl chains. Therefore, SAIL chemical architecture dictates: (1) how the density of neutral tails varies with the applied potential; and (2) how effective the self-assembled non-polar domains are for preventing overscreening. These two factors combined would ultimately determine the shape of the capacitance versus potential profile, which can provide direct information on the performance of SAILs and the desired operation voltages.

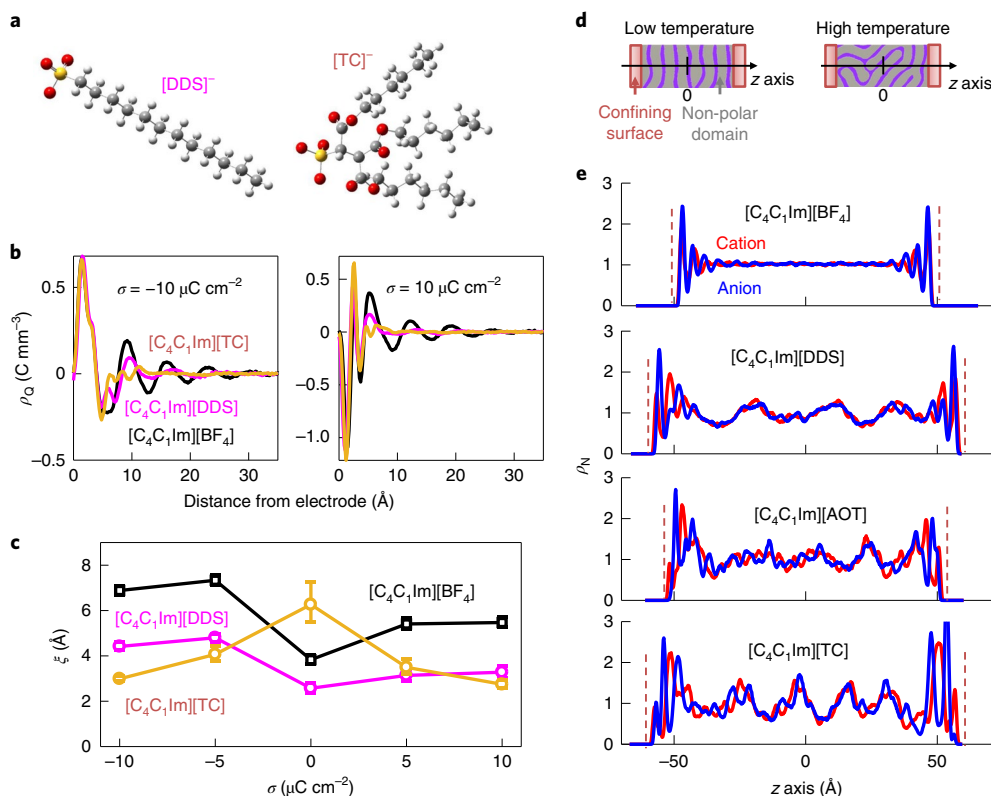


Fig. 5 | Molecular dynamics simulations of other SAILs. a, Molecular structures of $[\text{DDS}]^-$ and $[\text{TC}]^-$ (H, white; C, grey; S, yellow; O, red). **b,** ρ_Q profiles of $[\text{C}_4\text{C}_1\text{Im}][\text{DDS}]$, $[\text{C}_4\text{C}_1\text{Im}][\text{TC}]$ and $[\text{C}_4\text{C}_1\text{Im}][\text{BF}_4]$ at negatively (left panel) and positively charged interfaces (right panel). **c,** Decay length (ξ) versus σ for $[\text{C}_4\text{C}_1\text{Im}][\text{DDS}]$, $[\text{C}_4\text{C}_1\text{Im}][\text{TC}]$ and $[\text{C}_4\text{C}_1\text{Im}][\text{BF}_4]$. **d,** Schematic of the possible orientations of non-polar domains in SAILs at low (left) and high temperature (right). **e,** ρ_N profiles of $[\text{C}_4\text{C}_1\text{Im}][\text{BF}_4]$, $[\text{C}_4\text{C}_1\text{Im}][\text{DDS}]$, $[\text{C}_4\text{C}_1\text{Im}][\text{AOT}]$ and $[\text{C}_4\text{C}_1\text{Im}][\text{TC}]$ at 100 °C with zero charge on the confining surface. Dashed lines show the positions of the IL-solid interfaces.

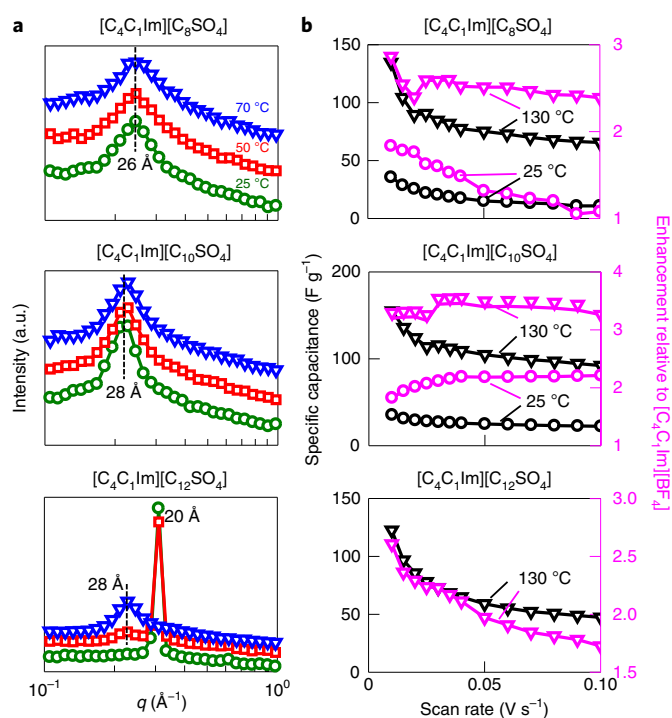


Fig. 6 | Electrocapacitive performances of other SAILs. **a**, SANS profiles of $[\text{C}_4\text{C}_1\text{Im}][\text{C}_8\text{SO}_4]$, $[\text{C}_4\text{C}_1\text{Im}][\text{C}_{10}\text{SO}_4]$ and $[\text{C}_4\text{C}_1\text{Im}][\text{C}_{12}\text{SO}_4]$ at 25, 50 and 70 °C. **b**, Specific capacitance (left y axes) versus the scan rate for $[\text{C}_4\text{C}_1\text{Im}][\text{C}_8\text{SO}_4]$ (25 and 130 °C), $[\text{C}_4\text{C}_1\text{Im}][\text{C}_{10}\text{SO}_4]$ (25 and 130 °C) and $[\text{C}_4\text{C}_1\text{Im}][\text{C}_{12}\text{SO}_4]$ (130 °C), together with enhancement factors (right y axes) compared with the performance of $[\text{C}_4\text{C}_1\text{Im}][\text{BF}_4]$.

In conclusion, this study reveals a fundamentally new interfacial phenomenon where the self-assembled nanostructures in ILs facilitate charge storage at electrified surfaces. This paves the way for building ‘designer’ SAILs, since there are a huge number of possible anion–cation combinations that can be employed to fine-tune the self-assembled nanostructures of SAILs and hence control interfacial electrochemical properties. Additionally, due to their exceptional stability and tunable electrochemical performance, rationally engineered SAILs could be used for a wide array of next-generation electrochemical devices for improved safety (for example, the avoidance of flammable organic electrolytes in batteries⁴²), and afford electrochemical modulation in vivo (for example, drug delivery⁴³) or for gas-based applications (for example, CO_2 capture⁴⁴, gas sensing⁴⁵ and biomimetic multiphase transport⁴⁶). More broadly, the self-assembly-based charge storage mechanism discovered here offers a new approach for optimizing the interfacial electrochemical behaviour of other fluids with ordered nanostructures beyond SAILs (for example, liquid crystals, block copolymer electrolytes and emulsions), and could have profound impacts on related emerging technologies.

Online content

Any methods, additional references, Nature Research reporting summaries, source data, statements of code and data availability and associated accession codes are available at <https://doi.org/10.1038/s41563-019-0449-6>.

Received: 19 October 2018; Accepted: 1 July 2019;

Published online: 12 August 2019

References

- MacFarlane, D. R. et al. Ionic liquids and their solid-state analogues as materials for energy generation and storage. *Nat. Rev. Mater.* **1**, 15005 (2016).

- Salanne, M. et al. Efficient storage mechanisms for building better supercapacitors. *Nat. Energy* **1**, 16070 (2016).
- Li, Y., Wang, X. G., Dong, S. M., Chen, X. & Cui, G. L. Recent advances in non-aqueous electrolyte for rechargeable Li– O_2 batteries. *Adv. Energy Mater.* **6**, 1600751 (2016).
- Armand, M., Endres, F., MacFarlane, D. R., Ohno, H. & Scrosati, B. Ionic-liquid materials for the electrochemical challenges of the future. *Nat. Mater.* **8**, 621–629 (2009).
- Che, H. Y. et al. Electrolyte design strategies and research progress for room-temperature sodium-ion batteries. *Energy Environ. Sci.* **10**, 1075–1101 (2017).
- Fedorov, M. V. & Kornyshev, A. A. Ionic liquids at electrified interfaces. *Chem. Rev.* **114**, 2978–3036 (2014).
- Bazant, M. Z., Storey, B. D. & Kornyshev, A. A. Double layer in ionic liquids: overscreening versus crowding. *Phys. Rev. Lett.* **106**, 046102 (2011).
- Gebbie, M. A., Dobbs, H. A., Valtiner, M. & Israelachvili, J. N. Long-range electrostatic screening in ionic liquids. *Proc. Natl Acad. Sci. USA* **112**, 7432–7437 (2015).
- Zhou, H. et al. Nanoscale perturbations of room temperature ionic liquid structure at charged and uncharged interfaces. *ACS Nano* **6**, 9818–9827 (2012).
- Gebbie, M. A. et al. Ionic liquids behave as dilute electrolyte solutions. *Proc. Natl Acad. Sci. USA* **110**, 9674–9679 (2013).
- Mezger, M. et al. Molecular layering of fluorinated ionic liquids at a charged sapphire (0001) surface. *Science* **322**, 424–428 (2008).
- Crowhurst, L., Lancaster, N. L., Arlandis, J. M. P. & Welton, T. Manipulating solute nucleophilicity with room temperature ionic liquids. *J. Am. Chem. Soc.* **126**, 11549–11555 (2004).
- Zhang, S. G., Zhang, J. H., Zhang, Y. & Deng, Y. Q. Nanoconfined ionic liquids. *Chem. Rev.* **117**, 6755–6833 (2017).
- Elbourne, A., Voitchovsky, K., Warr, G. G. & Atkin, R. Ion structure controls ionic liquid near-surface and interfacial nanostructure. *Chem. Sci.* **6**, 527–536 (2015).
- Lopes, J. N. A. C. & Padua, A. A. H. Nanostructural organization in ionic liquids. *J. Phys. Chem. B* **110**, 3330–3335 (2006).
- Padua, A. A. H., Gomes, M. F. & Lopes, J. N. A. C. Molecular solutes in ionic liquids: a structural perspective. *Acc. Chem. Res.* **40**, 1087–1096 (2007).
- Dong, K., Liu, X. M., Dong, H. F., Zhang, X. P. & Zhang, S. J. Multiscale studies on ionic liquids. *Chem. Rev.* **117**, 6636–6695 (2017).
- McDonald, S., Murphy, T., Imberti, S., Warr, G. G. & Atkin, R. Amphiphilically nanostructured deep eutectic solvents. *J. Phys. Chem. Lett.* **9**, 3922–3927 (2018).
- Brown, P. et al. Anionic surfactant ionic liquids with 1-butyl-3-methylimidazolium cations: characterization and application. *Langmuir* **28**, 2502–2509 (2012).
- Kim, Y. K., Wang, X. G., Mondkar, P., Bukusoglu, E. & Abbott, N. L. Self-reporting and self-regulating liquid crystals. *Nature* **557**, 539–544 (2018).
- Futamura, R. et al. Partial breaking of the Coulombic ordering of ionic liquids confined in carbon nanopores. *Nat. Mater.* **16**, 1225–1232 (2017).
- Mefford, J. T., Hardin, W. G., Dai, S., Johnston, K. P. & Stevenson, K. J. Anion charge storage through oxygen intercalation in LaMnO_3 perovskite pseudocapacitor electrodes. *Nat. Mater.* **13**, 726–732 (2014).
- Xia, Y. et al. Thickness-independent capacitance of vertically aligned liquid-crystalline MXenes. *Nature* **557**, 409–412 (2018).
- Zhong, C. et al. A review of electrolyte materials and compositions for electrochemical supercapacitors. *Chem. Soc. Rev.* **44**, 7484–7539 (2015).
- Smith, A. M. et al. Monolayer to bilayer structural transition in confined pyrrolidinium-based ionic liquids. *J. Phys. Chem. Lett.* **4**, 378–382 (2013).
- Kornyshev, A. A. Double-layer in ionic liquids: paradigm change? *J. Phys. Chem. B* **111**, 5545–5557 (2007).
- Pak, A. J., Paekw, E. & Hwang, G. S. Relative contributions of quantum and double layer capacitance to the supercapacitor performance of carbon nanotubes in an ionic liquid. *Phys. Chem. Chem. Phys.* **15**, 19741–19747 (2013).
- Merlet, C. et al. On the molecular origin of supercapacitance in nanoporous carbon electrodes. *Nat. Mater.* **11**, 306–310 (2012).
- Fedorov, M. V., Georgi, N. & Kornyshev, A. A. Double layer in ionic liquids: the nature of the camel shape of capacitance. *Electrochem. Commun.* **12**, 296–299 (2010).
- Georgi, N., Kornyshev, A. A. & Fedorov, M. V. The anatomy of the double layer and capacitance in ionic liquids with anisotropic ions: electrostriction vs. lattice saturation. *J. Electroanal. Chem.* **649**, 261–267 (2010).
- Perkin, S. et al. Self-assembly in the electrical double layer of ionic liquids. *Chem. Commun.* **47**, 6572–6574 (2011).
- Hayes, R., Warr, G. G. & Atkin, R. Structure and nanostructure in ionic liquids. *Chem. Rev.* **115**, 6357–6426 (2015).
- Espinosa-Marzal, R. M., Han, M., Arcifa, A., Spencer, N. D. & Rossi, A. in *Encyclopedia of Interfacial Chemistry* (ed. Wandelt, K.) 172–194 (Elsevier, 2018).

34. Werzer, O., Cranston, E. D., Warr, G. G., Atkin, R. & Rutland, M. W. Ionic liquid nanotribology: mica–silica interactions in ethylammonium nitrate. *Phys. Chem. Chem. Phys.* **14**, 5147–5152 (2012).
35. Voitchovsky, K. Anharmonicity, solvation forces, and resolution in atomic force microscopy at the solid–liquid interface. *Phys. Rev. E* **88**, 022407 (2013).
36. Lin, X., Salari, M., Arava, L. M. R., Ajayan, P. M. & Grinstaff, M. W. High temperature electrical energy storage: advances, challenges, and frontiers. *Chem. Soc. Rev.* **45**, 5848–5887 (2016).
37. Simon, P. & Gogotsi, Y. Capacitive energy storage in nanostructured carbon–electrolyte systems. *Acc. Chem. Res.* **46**, 1094–1103 (2013).
38. Pech, D. et al. Ultrahigh-power micrometre-sized supercapacitors based on onion-like carbon. *Nat. Nanotechnol.* **5**, 651–654 (2010).
39. Xie, K. et al. Carbon nanocages as supercapacitor electrode materials. *Adv. Mater.* **24**, 347–352 (2012).
40. Mao, X. et al. Microwave-assisted oxidation of electrospun turbostratic carbon nanofibers for tailoring energy storage capabilities. *Chem. Mater.* **27**, 4574–4585 (2015).
41. Mao, X. W., Simeon, F., Rutledge, G. C. & Hatton, T. A. Electrospun carbon nanofiber webs with controlled density of states for sensor applications. *Adv. Mater.* **25**, 1309–1314 (2013).
42. Li, J. C., Ma, C., Chi, M. F., Liang, C. D. & Dudney, N. J. Solid electrolyte: the key for high-voltage lithium batteries. *Adv. Energy Mater.* **5**, 1401408 (2015).
43. Alshammary, B., Walsh, F. C., Herrasti, P. & Ponce de Leon, C. Electrodeposited conductive polymers for controlled drug release: polypyrrole. *J. Solid State Electrochem.* **20**, 839–859 (2016).
44. Stern, M. C., Simeon, F., Herzog, H. & Hatton, T. A. Post-combustion carbon dioxide capture using electrochemically mediated amine regeneration. *Energy Environ. Sci.* **6**, 2505–2517 (2013).
45. Wang, L. D. et al. Molecular valves for controlling gas phase transport made from discrete angstrom-sized pores in graphene. *Nat. Nanotechnol.* **10**, 785–790 (2015).
46. Hou, X., Hu, Y. H., Grinthal, A., Khan, M. & Aizenberg, J. Liquid-based gating mechanism with tunable multiphase selectivity and antifouling behaviour. *Nature* **519**, 70–73 (2015).

Acknowledgements

This work was supported by an MIT Energy Initiative seed grant. X.M. acknowledges financial support from an MIT Skoltech fellowship. C.Č. acknowledges financial support from the Czech Science Foundation (GACR number 19-04150Y). C.Č. and

A.A.H.P. thank A. Dequidt of Université Clermont Auvergne for use of the computer program to calculate structure factors. We thank the UK research council STFC for providing beam time at the Institut Laue–Langevin, Grenoble, France. Small-angle neutron scattering experiments were supported under proposal number 9-12-434. X-ray reflectivity measurements were performed at Stanford Synchrotron Radiation Lightsources, SLAC National Accelerator Laboratory, which is supported by the US Department of Energy, Office of Science, Office of Basic Energy Sciences, under contract no. DE-AC02-76SF00515.

Author contributions

X.M. and P.B. conceived the initial idea. X.M. designed and led the research, carried out the electrochemical experiments, and analysed the experimental and simulation data, under the supervision of T.A.H. P.B. synthesized the SAILs and contributed to the electrochemical experiments, under the supervision of T.A.H. C.Č. carried out the molecular dynamics simulations under the supervision of A.A.H.P. and M.F.C.G. G.H. performed the SANS experiments under the supervision of J.E. and I.G. H.L. performed the AFM force measurements under the supervision of R.A. Y.R. contributed to the synthesis of the SAILs and X-ray reflectivity measurements. D.C. performed the X-ray reflectivity measurements. X.M. wrote the manuscript. All authors revised the manuscript.

Competing interests

X.M., P.B., M.F.C.G. and T.A.H. have filed a patent application based on this work (US Patent application number 16/323,468). This patent, entitled ‘High-temperature supercapacitors containing surface active ionic liquids’ was filed with the US Patent and Trademark Office on 5 February 2019, and published on 20 June 2019 with publication number US-2019-0189364-A1.

Additional information

Supplementary information is available for this paper at <https://doi.org/10.1038/s41563-019-0449-6>.

Reprints and permissions information is available at www.nature.com/reprints.

Correspondence and requests for materials should be addressed to X.M., M.F.C. or T.A.H.

Publisher’s note: Springer Nature remains neutral with regard to jurisdictional claims in published maps and institutional affiliations.

© The Author(s), under exclusive licence to Springer Nature Limited 2019

Methods

Synthesis of SAILs. 1-Butyl-3-methyl-imidazolium chloride ($[\text{C}_4\text{C}_1\text{Im}][\text{Cl}]$; $\geq 99\%$) was purchased from Sigma–Aldrich and used as received. Aerosol-OT (that is, sodium 1,4-bis(2-ethylhexoxy)-1,4-dioxobutane-2-sulfonate; also known as AOT) was purchased from Sigma–Aldrich, purified by Soxhlet extraction using dry acetone and subjected to repeated centrifugation. Ethyl acetate ($\geq 99.5\%$) was purchased from Sigma–Aldrich and used without further purification. The IL $[\text{C}_4\text{C}_1\text{Im}][\text{AOT}]$ was synthesized via an ion-exchange technique¹⁹ using a strong ion-exchange resin (Amberlite IR120 H⁺ form) as follows: surfactant (50 mmol sodium salt) was dissolved in 100 ml EtOH/H₂O (1:1 v/v) and passed through a column (20 cm \times 2 cm) of the ion-exchange resin. For the synthesis of $[\text{C}_4\text{C}_1\text{Im}][\text{C}_8\text{SO}_4]$, $[\text{C}_4\text{C}_1\text{Im}][\text{C}_{10}\text{SO}_4]$ and $[\text{C}_4\text{C}_1\text{Im}][\text{C}_{12}\text{SO}_4]$, sodium octyl sulfate ($>99.0\%$; $[\text{Na}][\text{C}_8\text{SO}_4]$), sodium decyl sulfate ($>99.0\%$; $[\text{Na}][\text{C}_{10}\text{SO}_4]$) and sodium dodecyl sulfate ($>99.0\%$; $[\text{Na}][\text{C}_{12}\text{SO}_4]$) were purchased from Sigma–Aldrich and used without further purification. These surfactants were also converted into ILs via an ion-exchange technique as for $[\text{C}_4\text{C}_1\text{Im}][\text{AOT}]$. Details of the synthesis and characterization of SAILs are presented in Supplementary Note 1.

SANS. Scattering was measured on the D33-massive dynamic q -range small-angle diffractometer at the Institut Laue–Langevin, Grenoble, France. A neutron wavelength of $\lambda = 10 \text{ \AA}$ was employed at two different detector distances, giving $0.0024 < Q < 0.37 \text{ \AA}^{-1}$. Data normalization using accepted procedures gave the absolute cross-section $I(Q) \text{ (cm}^{-1}\text{)}$ as a function of momentum transfer $Q \text{ (}\text{\AA}^{-1}\text{)}$. Samples were placed in Hellma fused silica cuvettes (path length: 2 mm). Additional data analysis procedures are discussed in Supplementary Note 2.

Electrochemical experiments. All electrochemical measurements of the supercapacitor devices were carried out with a VersaSTAT 4 potentiostat (Princeton Applied Research) in a two-electrode electrochemical cell thermostatted at the temperature of interest ($\pm 1 \text{ }^\circ\text{C}$). For the construction of the multi-walled CNT (MWCNT) supercapacitor devices⁴⁰, two pieces of MWCNT-deposited Toray carbon paper (active area: 2 cm \times 2 cm; mass loading: 2.67 mg cm⁻²) were assembled with VWR filter paper sandwiched between them as the separator. The entire assembly was then sandwiched between two microscope glass slides and dipped in the IL of interest. The two Toray carbon papers were attached to conductive copper tapes, which were connected to the potentiostat via alligator clips. The single-walled CNT and a.c. supercapacitor devices were assembled similar to MWCNTs. Electrochemical impedance measurements were performed in a three-electrode system that consisted of: (1) a flat-surface working electrode (either a glassy carbon electrode with a diameter of 3.0 mm or an Au electrode with 99.95% purity and a diameter of 3.0 mm); (2) an Ag/Ag⁺ reference electrode made of a silver wire, 10 mM AgBF₄, and the respective IL inside a glass tube with a porous CoralPor tip; and (3) a platinum gauze auxiliary electrode (90/10 platinum/iridium alloy; 50.0 mm height; 38.0 mm diameter). The heterogeneous electron transfer kinetics on the selected electrode were measured by sampled current voltammetry⁴⁷ using an electrolyte solution consisting of 1 mM Ru(NH₃)₆^{3+/2+} and 1.0 M KCl. Details of the electrochemical characterizations are presented in Supplementary Note 3.

Molecular dynamics simulation. The $[\text{C}_4\text{C}_1\text{im}]^+$ cation^{48,49} and $[\text{BF}_4]^-$ anion were represented by the Canongia Lopes and Pádua (CL&P) all-atom fixed charge force field⁵⁰. For the $[\text{AOT}]^-$, $[\text{DDS}]^-$ and $[\text{TC}]^-$ anions, the force field parameters were assembled from existing values of similar molecules containing sulfonate, ether and alkyl chain groups from the optimized potentials for liquid simulation, all-atom (OPLS-AA)^{51,52}, and are listed in Supplementary Tables 1–4. The atom types are illustrated in Supplementary Fig. 1. The graphite layers were modelled using the parameterization of Girifalco et al.⁵³. Molecular dynamics simulations were performed using the LAMMPS⁵⁴ software package with the Verlet integrator⁵⁵. Short-range forces (Lennard–Jones) were cut off at 12 \AA of interatomic separation, and long-range electrostatic forces were calculated with the particle–particle particle–mesh (PPPM)⁵⁶ method. The SHAKE algorithm⁵⁷ was employed to keep the lengths of the bonds terminating in hydrogen atoms constant, enabling us to use the time step of 1 fs for the simulations with a constant electrode charge density. Alternative simulations, during which the electrodes were kept at a

constant electrostatic potential difference, were run using the constant potential method developed by Siepman and Sprik⁵⁸ and Reed et al.⁵⁹, and implemented in LAMMPS by Wang et al.⁶⁰. Details of the molecular dynamics simulations are presented in Supplementary Note 4.1.

AFM. Force–distance profiles were performed using a Veeco NanoScope IV AFM. Three sharp silicon cantilevers (spring constant: $0.3 \pm 0.1 \text{ N m}^{-1}$) from the same batch (model NSC36; Mikromasch) were used over the course of the investigation. The cantilevers were cleaned before use by careful rinsing in Milli-Q water and ethanol, drying under nitrogen, and irradiation with ultraviolet light for 20 min. An AFM electrochemistry fluid cell (MMTMEC; Bruker) was used to hold ILs on a highly oriented pyrolytic graphite surface during the measurements. Highly oriented pyrolytic graphite was used as both the working electrode and the solid substrate for AFM measurements. Pt wires of 0.25 mm were used as both the counter and ‘quasi’ reference electrodes. More details on the AFM measurements can be found in Supplementary Note 5.

Data availability

The data that support the findings of this study are available from the corresponding authors upon reasonable request.

References

- Mao, X., Guo, F., Yan, E. H., Rutledge, G. C. & Hatton, T. A. Remarkably high heterogeneous electron transfer activity of carbon-nanotube-supported reduced graphene oxide. *Chem. Mater.* **28**, 7422–7432 (2016).
- Canongia Lopes, J. N., Deschamps, J. & Pádua, A. A. H. Modeling ionic liquids using a systematic all-atom force field. *J. Phys. Chem. B* **108**, 2038–2047 (2004).
- Kaminski, G. A. & Jorgensen, W. L. Host–guest chemistry of rotaxanes and catenanes: application of a polarizable all-atom force field to cyclobis(paraquat-*p*-phenylene) complexes with disubstituted benzenes and biphenyls. *J. Chem. Soc. Perkin Trans. 2*, 2365–2375 (1999).
- Canongia Lopes, J. N. & Pádua, A. A. H. CL&P: a generic and systematic force field for ionic liquids modeling. *Theor. Chem. Acc.* **131**, 1129 (2012).
- Canongia Lopes, J. N., Pádua, A. A. H. & Shimizu, K. Molecular force field for ionic liquids IV: trialkylimidazolium and alkoxy carbonyl-imidazolium cations; alkylsulfonate and alkylsulfate anions. *J. Phys. Chem. B* **112**, 5039–5046 (2008).
- Price, M. L. P., Ostrovsky, D. & Jorgensen, W. L. Gas-phase and liquid-state properties of esters, nitriles, and nitro compounds with the OPLS-AA force field. *J. Comput. Chem.* **22**, 1340–1352 (2001).
- Girifalco, L. A., Hodak, M. & Lee, R. S. Carbon nanotubes, buckyballs, ropes, and a universal graphitic potential. *Phys. Rev. B* **62**, 13104–13110 (2000).
- Plimpton, S. Fast parallel algorithms for short-range molecular dynamics. *J. Comp. Phys.* **117**, 1–19 (1995).
- Tuckerman, M. E., Alejandre, J., Lopez-Rendon, R., Jochim, A. L. & Martyna, G. J. A liouville-operator derived measure-preserving integrator for molecular dynamics simulations in the isothermal-isobaric ensemble. *J. Phys. A Math. Gen.* **39**, 5629–5651 (2006).
- Hockney, R. W. & Eastwood, J. W. *Computer Simulation Using Particles* (Taylor & Francis, 1988).
- Ryckaert, J. P., Ciccoliti, G. & Berendsen, H. J. C. Numerical integration of the cartesian equations of motion of a system with constraints—molecular dynamics of *n*-alkanes. *J. Comp. Phys.* **23**, 327–341 (1977).
- Siepman, J. I. & Sprik, M. Influence of surface topology and electrostatic potential on water/electrode systems. *J. Chem. Phys.* **102**, 511–524 (1995).
- Reed, S. K., Lanning, O. J. & Madden, P. A. Electrochemical interface between an ionic liquid and a model metallic electrode. *J. Chem. Phys.* **126**, 084704 (2007).
- Wang, Z., Yang, Y., Olmsted, D. L., Asta, M. & Laird, B. B. Evaluation of the constant potential method in simulating electric double-layer capacitors. *J. Chem. Phys.* **141**, 184102 (2014).